Revision 1

Recoil-free Fractions of Iron in Aluminous Bridgmanite from Temperature Dependent Mössbauer Spectra

Jiachao Liu[1], Bjorn Mysen[2], Yingwei Fei[2], Jie Li[1]

1. Department of Earth and Environmental Sciences, University of Michigan, Ann Arbor, MI 48109, USA
2. Geophysical Laboratory, Carnegie Institution of Washington, Washington, DC 20015, USA

Abstract

Aluminous bridgmanite (Al-Bm) is the dominant phase in the Earth's lower mantle. In this study, the Mössbauer spectra of an Al-Bm sample $Mg_{0.868}Fe_{0.087}Si_{0.944}Al_{0.101}O_{2.994}$ were recorded from 65 K to 300 K at 1 bar. The temperature dependence of the center shift was fitted by the Debye model and yielded the Debye temperatures of 305±3 K for Fe^{2+} and 361±22 K for Fe^{3+}. These values are lower than those of Al-free bridgmanite by 17% and 24%, respectively, indicating that the presence of Fe and Al increases the average Fe-O bond length and weakens the bond strength. At 300 K, the calculated recoil-free fractions of Fe^{2+} (0.637±0.006) and Fe^{3+} (0.72±0.02) are similar and therefore the molar fractions of Fe^{2+} and Fe^{3+} are nearly the same as the area fractions of the corresponding Mössbauer doublets. At 900 K, the calculated recoil-free fractions of Fe^{3+} is 46% higher than that of Fe^{2+}, implying that the molar fraction of Fe^{3+} is only 4 1% for a

Always consult and cite the final, published document. See http://www.minsocam.org or GeoscienceWorld

measured spectral area fraction of 50%, and that the area fractions of iron sites may change with temperature without any changes in the valence state or spin state of iron. We infer that Fe^{3+} accounts for 46±2 % of the iron in the Al-Bm and it enters the A site along with Al^{3+} in the B site through the coupled-substitution mechanism. An Fe^{2+} component with large QS ~4.0mm/s was observed at cryogenic conditions and interpreted as a high-spin distorted iron site.

Keywords: Mössbauer spectroscopy, aluminous bridgmanite, ferric iron, recoil-free fraction, Debye temperature, crystallographic site, lower mantle

1. Introduction

Aluminum- and iron-bearing magnesium silicate bridgmanite (abbreviated as "Al-Bm", following the same convention as Rw for ringwoodite) is the predominant phase in the Earth's lower mantle, and its physical properties and crystal chemistry play an important role in mantle dynamics. Iron, with a partially filled 3d shell, adds a variety of influences to the physical properties and chemical behavior of Bm. The oxidation state, spin state, and site occupancy of iron in Bm are of particular importance because these factors may influence the density and velocity structure and convective pattern of the lower mantle (e.g., Badro 2014; Li 2007; Lin et al. 2013)

Mössbauer spectroscopy probes the hyperfine interactions between the nuclei/nucleus and the surrounding electric and magnetic fields. These interactions are expressed as center shift (CS), quadrupole splitting (QS), and the magnetic Zeeman splitting. Mössbauer spectroscopy also has been widely used to measure the valence state of iron in geological materials (Dyar et al., 2006). In the past two decades, Mössbauer spectroscopy has been applied to investigating the valence state, spin state and crystal chemistry of iron

Always consult and cite the final, published document. See http://www.minsocam.org or GeoscienceWorld

in lower-mantle Bm (e.g., Fei et al. 1994; McCammon 1997, 1998; Jackson et al. 2005; Li et al. 2006; Lin et al. 2012; Bengtson et al. 2009; Narygina et al. 2010; Grocholski et al. 2009; Catalli et al. 2010; Hummer and Fei 2012). Of particular importance are Mössbauer measurements at variable temperatures, which provide information on recoil-free fractions (*f*) of different iron sites and thus allow for reliable determination of the relative proportions of divalent and trivalent iron. Moreover, effects of temperature on the hyperfine parameters have been used to test the validity of the fitting procedure of Mössbauer data, and to gain additional insights on electron delocalization in Al-free Bm at elevated temperatuers (Fei et al. 1994; McCammon 1998).

Bridgmanite in the lower mantle contains 4.0~5.3 weight % Al (Wood and Rubie 1996). The presence of Al alters the crystal chemistry of iron and appears to stabilize trivalent iron in the structure (McCammon 1997; Frost et al. 2004). Such structural changes may also affect the recoil-free fractions of both Fe^{2+} and Fe^{3+}, which need to be determined in order to derive the Fe^{3+}/Fe ratios from Mössbauer spectra. Mössbauer data of Al-Bm under cryogenic conditions appear not to have been reported. In this study, we measured Mössbauer spectra of an Al-Bm sample from 65 to 300 K at 1 bar and applied the results to examine the crystal chemistry of Fe^{2+} and Fe^{3+} in lower mantle Bm.

2. Experimental Method

2.1. Sample Synthesis and Characterization

An Al-Bm sample was synthesized and characterized at the Geophysical Laboratory, Carnegie Institution of Washington. The synthesis procedure started with reducing a 94% ^{57}Fe enriched Fe_2O_3 to FeO at 1273 K and $\log f_{O2}$ = -14 (between the iron-wüstite and wüstite-magnetite buffers) for 24 hours in a CO-CO_2 gas-mixing furnace to reduce all

Always consult and cite the final, published document. See http://www.minsocam.org or GeoscienceWorld

Fe^{3+} to Fe^{2+}. An $(Mg_{0.9}Fe_{0.1})(Si_{0.9}Al_{0.1})O_3$ orthopyroxene was then synthesized by equilibrating the stoichiometric mixture of MgO, SiO_2, FeO and Al_2O_3 in a graphite capsule at 2 GPa and 1673 K for 3 days in a piston cylinder apparatus. A Mössbauer spectrum of this sample shows all iron in orthopyroxene to be Fe^{2+}. Several milligrams of the orthopyroxene were packed into a rhenium capsule and equilibrated at 26.5 GPa and 2023 K for 30 minutes with a multi-anvil apparatus by using methods described by Bertka and Fei (1997)**.** The recovered run product was crushed between two tungsten carbide (WC) anvils at 77 K to minimize back transformation or amorphization. The average composition of the synthesized Al-Bm, determined with the JEOL 8900 electron microprobe at the Geophysical Laboratory, is $Mg_{0.868(11)}Fe^{2+}_{0.087(5)}Si_{0.944(10)}Al_{0.101(3)}O_{2.994}$ as formulated on the two- cation basis and assuming all iron to be ferrous The structure and purity of the run product were further confirmed by an energy-dispersive powder X-ray diffraction (XRD) pattern collected at the GSECARS of the Advanced Photon Source, Argonne National Laboratory, and by a Raman spectrum collected at the Geophysical Laboratory, which matched the existing references (Bertka and Fei 1997). Ferropericlase was not detected in the electron microprobe, or XRD measurements. The absence of ferropericlase is consistent with the excess SiO_2 in the starting composition and the presence of a smaller amount of stishovite in the run product.

2.2. Conventional Mössbauer Spectroscopy

Mössbauer spectra of Al-Bm were acquired at temperatures between 65 and 300 K at the Geophysical Laboratory, following the method described in Fei et al. (1994). A closed-cycle refrigerator was used to generate cryogenic temperatures. For Mössbauer measurements, a 0.5” or ~12 mm-diameter pellet was prepared by mixing the crushed

Always consult and cite the final, published document. See http://www.minsocam.org or GeoscienceWorld

sample with transoptic binder, which was sandwiched between two sheets of high-purity alumina foil. This sample was placed between the faces of two Cu discs with a 0.75-in or ~ 19 mm aperture, each lined with indium foil and attached to the cold finger of the cryostat. Temperature was monitored with a chromel alumel thermocouple next to the sample. An Austin Science Drive operating in the constant acceleration mode produced velocities in the range of ±4 mm/s. The Mössbauer absorption intensity was collected over 512 channel in a mirror-imaged mode. The velocity-channel relation was calibrated using the inner four lines of the stainless steel sextet. The gamma-ray source was a 30 mCi Co in Pd matrix. Spectra were first collected at the lowest temperature of 65 K, and then at progressively higher temperature until reaching the room temperature.

3. Results and Discussions

The Mössbauer spectra (Fig. 1) do not show evidence of metallic Fe, which would produce a sextet associated with magnetic Zeeman splitting. The absence of metallic Fe was also indicated from examination of electron back-scattered images. Accordingly, we fitted the spectra by multiple doubles with Lorentzian line shape using the fitting program "MossA" (Prescher et al. 2012).

To account for the main feature of each spectrum (Fig. 1), we first introduced two doublets with distinct quadruple splitting (QS) values, corresponding to one Fe^{2+} site and one Fe^{3+} site, respectively. The broad and asymmetric absorption peaks near -1 mm/s and 2 mm/s suggest the presence of a second Fe^{2+} doublet. A small peak near 3 mm/s requires a third Fe^{2+} doublet with unusually large quadrupole splitting value, exceeding 4 mm/s. The central shift (CS) of the Fe^{2+}III doublet is well constrained and its value falls into the range of CS for Fe^{2+} in minerals (Dyar et al. 2006). The Fe^{2+}II doublet has an

Always consult and cite the final, published document. See http://www.minsocam.org or GeoscienceWorld

anomalously large width. Treatment of this doublet with a Voigt-based function involving correlated QS and CS distributions (Lagarec and Rancourt 1997) did not improve the fits based on the F test. We chose, therefore, to keep Fe^{2+}II as a Lorentzian doublet. The line shape of Fe^{2+}II did not affect its own hyperfine parameters but influenced those of Fe^{3+} because the low-velocity peak of the Fe^{3+} doublet overlaps with other peaks. The Fe^{2+}II doublet are broader than those reported in the literature (e.g., Fei et al. 1994). With the maximum full width at half maximum (FWHM) of the Fe^{2+}II constrained to a typical value of 0.6 mm/s, the derived Fe^{3+}/Fe ratio decreases by 10% between 65 K and 300 K. This approach is discarded because the valence state of iron is unlikely to change under the cryogenic conditions. We interpret the broad line widths as a manifestation of complexity in the local electronic environment of iron site (Bengtson et al. 2009). With increasing temperature, the relative area of the Fe^{2+}II doublet increased at the expense of the Fe^{2+}I doublet and the large QS site (Fe^{2+}III doublet), with the combined area of all three Fe^{2+} sites remaining nearly constant (Fig. 2). Previous studies used an additional doublet to fit systematic aberrations near 1.2~1.3 mm/s (Fei et al. 1994; McCammon 1998) and attributed this component to Fe^{2+}-Fe^{3+} electron delocalization. We did not find it necessary to introduce this component (Fig. 1). Furthermore, the fitted CS of each site from our fits decreases with increasing temperature (Fig. 2d), as expected for the second-order Doppler shift (Fei et al. 1994). The areas of Fe^{3+} and total Fe^{2+} are constant within uncertainties over the temperature range investigated (Table 1). All the above evidence supports the conclusion that Fe^{2+}-Fe^{3+} electron delocalization does not happen in the Al-Bm sample examined here.

3.1. The Recoil-free Fractions of Fe^{2+} and Fe^{3+} in Al-Bm

Always consult and cite the final, published document. See http://www.minsocam.org or GeoscienceWorld

As Fe^{2+} and Fe^{3+} have different valence states and may occupy different crystallographic sites, the recoil-free fractions of Fe^{2+} and Fe^{3+}, denoted as f_2 and f_3, respectively, are generally unequal. Knowledge of the recoil-free fractions is necessary to convert the Mössbauer spectral areas of iron sites to their molar fractions. According to the harmonic theory of lattice dynamics, the recoil-free fraction, f (also known as Lamb-Mössbauer factor), decreases with the mean square displacement of the Mössbauer isotope from its equilibrium position $\langle x^2 \rangle$ and depends on the wavelength of the gamma photons, λ, through the equation $f = \exp(-4\pi^2 \langle x^2 \rangle / \lambda^2)$ (Frauenfelder 1962). By using the Debye approximation for lattice vibration, the recoil free fraction at a given temperature $f(T)$ is commonly calculated from the characteristic Debye temperature Θ_D according to:

$$f(T) = \exp\left\{-\frac{3}{2}\frac{E_R}{k_B\Theta_D}\left[1 + 4\left(\frac{T}{\Theta_D}\right)^2 \int_0^{\Theta_D/T} \frac{x\,dx}{e^x - 1}\right]\right\}$$

where the recoil energy E_R is 3.13425×10^{-22} J for the 14.4 keV gamma ray from the decay of ^{57}Co to stable ^{57}Fe, and k_B is the Boltzmann constant (Pound and Rebka 1960). Given Mössbauer data at variable temperatures, the Θ_D can be determined by fitting the temperature-dependent center shift $\delta(T)$ to the following relation:

$$\delta(T) = \delta_I - \frac{9}{2}\frac{k_B T}{Mc}\left(\frac{T}{\Theta_D}\right)^3 \int_0^{\Theta_D/T} \frac{x^3\,dx}{e^x - 1}$$

Where δ_I is the intrinsic isomer shift, M is the mass of the Mössbauer nucleus, and c is the velocity of light in vacuum. For the Al-Bm sample, we fitted the CS of Fe^{3+}, Fe^{2+}III, and the weighted average of Fe^{2+}I and Fe^{2+}II to the above equation and derived the δ_I and Θ_D values and the corresponding f at 300 K for each site (Fig. 2d, Table 2).

Always consult and cite the final, published document. See http://www.minsocam.org or GeoscienceWorld

158 For a given site *i*, the relation between its molar fraction, x_i, and Mössbauer spectral area
159 fraction, A_i, is $x_i = (A_i/f_i)/\Sigma(A_i/f_i)$. The recoil free fraction of Fe^{2+} f_2 and that of Fe^{3+}
160 f_3 derived from our data are similar between 65 and 300 K (Table 2 and Fig. 3).
161 Therefore, the molar fraction of trivalent iron with respect to total iron (Fe^{3+}/Fe =
162 46±2%) is indistinguishable from its spectral area fraction of 49±2% (Table 1).
163 According to the Debye model, both f_2 and f_3 of the Al-Bm become considerably smaller
164 and diverge from each other at higher temperatures (Fig. 3). At 900 K, the calculated f_3 is
165 46% higher than f_2, implying that the molar fraction of Fe^{3+} is only 41% for a measured
166 spectral area fraction of 50%, and that the area fractions of iron sites may change with
167 temperature without any changes in the valence state or spin state of iron.

168 **3.2. Crystal Chemistry**

169 Knowledge of the site occupancy of iron in Bm is essential to understand the
170 chemistry and physics of the lower mantle, including the nature of spin crossover and the
171 mechanism of thermal and electrical conduction (e.g. Badro 2014; Li 2007; Lin et al.
172 2013). According to experimental observations and atomistic calculations, Fe^{2+} occupies
173 the pseudo-dodecahedral or A site through simple substitution: $Fe^{2+}_A = Mg^{2+}_A$ (e.g.,
174 Wright and Price, 1989). A number of mechanisms have been proposed for the site
175 occupancy of Fe^{3+} (Frost and Langenhorst 2002; Frost et al. 2004; Lauterbach et al. 2000;
176 Hummer and Fei 2012). Given the knowledge of chemical composition and the Fe^{3+}
177 fraction we may use the $(Fe,Mg)_2O_2$-$(Fe^{3+},Al)_2O_3$-Si_2O_4 ternary diagram to infer the site
178 occupancies of Fe^{3+} in Bm (Fig. 4). In compositions that plot along the $(Fe^{3+},Al)_2O_3$ and
179 $(Mg,Fe^{2+})SiO_3$ join, Fe^{3+} likely enters either the A site or the octahedral B site through
180 substitution of two trivalent ions for Mg^{2+} in the A site and Si^{4+} in the B site: Mg^{2+}_A +

Always consult and cite the final, published document. See http://www.minsocam.org or GeoscienceWorld

$Si^{4+}_B = Fe^{3+}_A + (Fe^{3+},Al^{3+})_B$, known as the coupled substitution mechanism. In compositions showing oxygen deficiency, Fe^{3+} may have substituted for Si^{4+} in the B site and is charge balance by introducing a vacancy in the oxygen site (V_O): $2Si^{4+} + O^{2-} = 2Fe^{3+} + V_O$, known as the oxygen vacancy substitution mechanism. For compositions with excess oxygen, Fe^{3+} may have substituted for Mg^{2+} in the A site and is charge-balanced by removing an extra Mg^{2+} which produces an apparent excess in oxygen: $2Fe^{3+} = 3Mg^{2+}$, known as the cation vacancy substitution mechanism. As an alternative to removing an extra Mg^{2+}, charge balance may be maintained by introducing an interstitial oxygen, which is considered energetically unfavorable (Smyth 1993).

Bm compositions that were synthesized at different pressure and temperature conditions spread over a broad range in the $(Fe,Mg)_2O_2$-$(Fe^{3+},Al)_2O_3$-Si_2O_4 ternary diagram, indicating variable site occupancy of iron in the structure (Fig. 4). This is consistent with the previous findings that the synthesis condition influences the volume and compressibility of Bm, as well as its spin-pairing transition behavior (Catalli et al. 2010; Fujino et al. 2012; Hummer and Fei 2012; Lundin et al. 2008).

Using the ternary diagram, we infer that most Al-free Bm compositions in the literature involve a combination of coupled substitution and cation vacancy substitution. Those synthesized in very oxidizing environment are exceptions and scattered significantly in this plot (Hummer and Fei 2012). Relatively large uncertainty in Fe^{3+} content also results in wide scatter (Frost and Langenhorst 2002).

The situation is more complex in Al-Bm (Frost et al. 2004; Richmond and Brodholt 1998). Whereas the majority of Al-Bm involve the oxygen vacancy substitution and coupled substitution mechanisms (Fig. 4), the Al-Bm sample from our study and that of

Always consult and cite the final, published document. See http://www.minsocam.org or GeoscienceWorld

Narygina et al. (2009) plot between the joins (2) and (3), indicating that some trivalent cations entered the structure through the cation vacancy mechanism. Richmond and Brodholt (1998) showed that the most favorable mechanism to incorporate trivalent cations in the Bm structure is through the coupled substitution $Mg^{2+}_{A} + Si^{4+}_{B} = Fe^{3+}_{A} + Al^{3+}_{B}$, where Fe^{3+} and Al^{3+} substitute into adjacent sites. Given that the Al^{3+}/Fe^{3+} ratio of the Al-Bm is larger than one, we infer that all the Fe^{3+} occupies the A site, coupled with an equal fraction of Al^{3+} in the B site. Because the Mg/Si ratio of the sample is smaller than one, some of the remaining Al^{3+} may adopt the A site through the cation vacancy mechanism in order to approach an equal distribution of cations in the two sites. The inferred occupancy of Fe^{3+} in the A site alone is consistent with the narrow width of the corresponding doublet (Fig. 1 and Table 1), and with the absence of Fe^{n+} in our sample. Previous studies interpreted Fe^{n+} as a result of electron hopping between Fe^{2+} and Fe^{3+}, which likely occurs between the adjacent A and B sites the cation-cation distance falling within the range for electron hopping in oxides and silicates (Fei et al. 1994, McCammon 1998). In contrast, the cation-cation distance between adjacent A sites is marginally within the range of electron hopping and hence less likely to occur. Note that the presence of Fe^{3+} in the Al-Bm cannot be inferred from the composition alone because its influence on the cation to oxygen ratio depends on how trivalent ions are incorporated in the structure: The ratio would exceed the stoichiometric value of 2 to 3 if trivalent ions preferentially enters the A site, fall below the value if they preferentially enters the B site, or does not change if all trivalent ions enters both sites in equal proportion through the coupled substitution mechanism.

3.3. Debye Temperature

Always consult and cite the final, published document. See http://www.minsocam.org or GeoscienceWorld

Even though the physical meaning of Debye temperature Θ_D, derived from Mössbauer measurements, is not fully understood, it is generally accepted that it can be used to compare the strength of chemical bonding among structurally related compounds (De Grave et al. 1985). McCammon (1998) reported the Debye temperatures of an Al-free Bm (Table 2). We were able to exactly reproduce the results, thus confirming the validity of the fitting procedure. Compared with the Al-free Bm, the Debye temperatures of Fe^{2+} and Fe^{3+} in the Al-Bm are lower by 17% and 24%, respectively, resulting in f_2 and f_3 values at 300 K that differ by 13 % (Table 2). The lower Debye temperatures in Al-Bm are consistent with the finding that substituting larger Al^{3+} ion for smaller Si^{4+} ion in the B site expands its volume and increases the average bond length (Lundin et al. 2008; Vanpeteghem et al. 2006). Moreover, this substitution causes tilting of the octahedra, therefore, inflates the A site. The elongated and weakened Fe-O bond then give rise to the lower Debye temperatures and smaller recoil free fractions, f_2 and f_3, in Al-Bm.

One intriguing phenomenon is that the fitted Debye temperature of the Fe^{2+}III site exceeds 1000 K (Table 2) and is more than twice the highest value reported in the literature (De Grave and Van Alboom 1991). Unlike the very large values of Debye temperatures for Fe^{2+} in Al-free Bm samples (Fei et al. 1994), which have been attributed to fitting artifacts (McCammon 1998), the unusually high Debye temperature is a robust feature because the CS values of the Fe^{2+}III doublets are well constrained by the Mössbauer data. Theoretical calculations have shown that at 0.1 MPa two high-spin (HS) Fe^{2+} sites with distinct QS values exist in the A site of Bm, and the one with a large QS value (~ 3.2 mm/s) has a shorter average bond length (Bengtson et al. 2009; Hsu et al. 2010). This is consistent with the observation that Fe^{2+}III with large QS has

Always consult and cite the final, published document. See http://www.minsocam.org or GeoscienceWorld

extraordinarily high Debye temperatures, reflecting its short bond length and high bond strength.

3.4. The Fe^{2+} Site with Large QS

Recent Mössbauer studies detected Fe^{2+} sites with extremely large QS values (~4.0 mm/s) at pressures above 30 GPa (Kupenko et al. 2014; Lin et al. 2008; McCammon et al. 2008; Narygina et al. 2010; Potapkin et al. 2013). These values were interpreted to be the results of intermediate-spin (IS) Fe^{2+} according to the spin numbers derived from X-ray emission spectroscopy data (Lin et al. 2008), or attributed to high-spin (HS) Fe^{2+} (Grocholski et al. 2009; Jackson et al. 2005; Li et al. 2004, 2006; Lin et al. 2012). Theoretical calculations suggested that IS Fe^{2+} is unstable relative to HS or low-spin (LS) Fe^{2+} and that the QS of the intermediate-spin Fe^{2+} in the A site falls into the range of 0.7 to 1.4 mm/s, which is well below 4.0 mm/s (Bengtson et al. 2009; Hsu et al. 2010). Additionally, these studies showed that HS Fe^{2+} in the A site could have high QS (3.2-3.6 mm/s) due to difference in d-orbital occupation and local distortion.

In the Al-Bm, the Fe^{2+}III site has similar QS-values (3.47-4.03 mm/s) and CS-values (~1.1 mm/s) to those proposed for IS Fe^{2+} (Kupenko et al. 2014; Lin et al. 2008; McCammon et al. 2008; Narygina et al. 2010; Potapkin et al. 2013), and its area fraction in the Mössbauer absorption spectra decreased with temperature from 6% at 65 K to near 0% at 300 K (Table 1). It is generally understood that the high-spin state is favored at low pressures and/or high temperatures. A potential explanation for the large QS and temperature dependence of the Fe^{2+} III site is, therefore, that it represents an IS or LS-site at low temperatures, which transforms to a HS state as temperature rises. To test this hypothesis, we estimated the temperature of spin-pairing transition at 0.1 MPa, on the

Always consult and cite the final, published document. See http://www.minsocam.org or GeoscienceWorld

basis of simplified crystal field theory and existing data on pressure-induced spin-pairing transition in Bm at 300 K. The spin transition at 65 K is expected to take place below 30 GPa as a result of the entropy difference between IS (or LS) and HS iron (dS) and thermal contraction. By assuming the crystal field splitting energy (CFSE), Δ, relates to the Fe-O bond length, R, through $\Delta \sim R^{-5}$ (Burns 1993) and ignoring the volume difference between the adjacent spin states (Catalli et al. 2010; Lundin et al. 2008), for a temperature drop of dT, the spin transition pressure would decrease by $dT \bullet dS/(5n\Delta/3K_T)$ because of the entropy difference, and by $(\alpha K_T dT)_V$ because of thermal contraction, where n is the number of electrons that flip spin through the transition, K_T is the isothermal bulk modulus, and α is the isobaric thermal expansion coefficient. By using the parameters in Li (2007), we found that the pressure of HS to LS transition of Fe^{2+} at 65 K is 1.7 GPa lower than that at 300 K, where 0.4 GPa is from the entropy and 1.3 GPa from thermal contraction. From HS to IS, the transition pressure at 65 K is 3.1 GPa lower, where 1.8 GPa comes from the entropy effect and 1.3 GPa from the thermal contraction effect. Given the pressures of spin transitions in Bm at 300 K range from 30 to 120 GPa (e.g., Badro et al. 2004; Fujino et al. 2012; Catalli et al. 2010; McCammon et al. 2010; Jackson et al. 2005; Li et al. 2006), and that these pressures would only be lowered by a few GPa, we conclude that the Fe^{2+}III site represents a HS state and that the large QS likely result from temperature-induced change in the degree of lattice distortion (Bengtson et al. 2009; Hsu et al. 2010).

4. Implications

Always consult and cite the final, published document. See http://www.minsocam.org or GeoscienceWorld

For an Al- and Fe-bearing Bm sample with a composition that is applicable to the Earth's lower mantle, we found that the recoil-free fractions of Fe^{2+} and Fe^{3+} at 300 K are 0.637 and 0.72, respectively. These values are sufficiently similar so that the molar fractions of the two ions can be roughly equated to the area fractions of their respective Mössbauer doublet. By using the fitted Debye temperatures to calculate the recoil-free fractions at different temperatures we expect the recoil-free fraction of Fe^{3+} at 900 K to be 46% higher than that of Fe^{2+} because of different temperature dependence, thus requiring a downward correction to calculate the molar fraction of Fe^{3+} from its area fraction in the Mössbauer spectra.

Contrary to some of the recent studies that interpreted exceptionally large QS value as a diagnostic feature of intermediate spin state of iron in Bm, we observed a Fe^{2+} component with a large QS near 4.0mm/s at 1 bar and below 250 K, which supports the theoretical prediction of large QS resulting from distortion rather than spin-crossover.

Our analyses of a large number of Bm samples reported in the literature suggest that site occupancy of Fe^{3+} depends on Al content and synthesis conditions: Whereas the majority of the Al-free samples can be explained by a combination of coupled substitution and cation vacancy substitution, a combination of coupled substitution and oxygen vacancy mechanism is inferred for most of the Al-bearing samples.

The geophysical estimate of the lower-mantle electric conductivity has been adequately explained by the Bm component (e.g., Katsura et al. 1998). It was shown that at temperatures up to 1500 K conduction mechanism was dominated by Fe^{2+}-Fe^{3+} electron hopping with relatively small activation energy, whereas at higher temperatures the dominant mechanism is ionic conduction through A site vacancies and oxygen

Always consult and cite the final, published document. See http://www.minsocam.org or GeoscienceWorld

vacancies, which involves larger activation energy (Katsura et al. 1998; Xu and McCammon 2002). In the Al-Bm at 300 K examined here, Fe^{3+} was found to exclusively enter the pseudo-dodecahedral A site through the coupled substitution mechanism, which is consistent with the Mössbauer results that indicate no electron hopping. Accordingly the Al-Bm is expected to have low electric conductivity at ambient conditions. A recent study on spin crossover suggested that at pressures above 50-60 GPa and high temperatures, Fe^{3+} in the A site exchanged with Al^{3+} in the B sites and transitioned to the low-spin state (Fujino et al. 2012). Such migration would enable electron hopping between Fe^{2+} in the A site and low-spin Fe^{3+} in the B site and therefore lower the activation energy and increase the electric conductivity of the Al-Bm.

References

Badro, J. (2014) Spin transitions in mantle minerals. Annual Review of Earth and Planetary Sciences, 42, 231-248.

Badro, J., Rueff, J.P., Vanko, G., Monaco, G., Fiquet, G., and Guyot, F. (2004) Electronic transitions in perovskite: possible nonconvecting layers in the lower mantle. Science, 305, 383-386.

Bengtson, A., Li, J., and Morgan, D. (2009) Mössbauer modeling to interpret the spin state of iron in $(Mg,Fe)SiO_3$ perovskite. Geophysical Research Letters, 36, L15301.

Bertka, C. M., and Y. Fei (1997) Mineralogy of the Martian interior up to core-mantle boundary pressures, J. Geophys. Res., 103, 5251-5264.

Burns, R.G. (1993) Mineralogical Applications of Crystal Field Theory, Seond ed., Cambridge University Press, Cambridge, p. 551.

Always consult and cite the final, published document. See http://www.minsocam.org or GeoscienceWorld

Catalli, K., Shim, S.H., Prakapenka, V.B., Zhao, J.Y., Sturhahn, W., Chow, P., Xiao, Y.M., Liu, H.Z., Cynn, H., and Evans, W.J. (2010) Spin state of ferric iron in $MgSiO_3$ perovskite and its effect on elastic properties. Earth and Planetary Science Letters, 289, 68-75.

De Grave, E., and Van Alboom, A. (1991) Evaluation of ferrous and ferric Mössbauer fractions. Physics and Chemistry of Minerals, 18, 337-342.

De Grave, E., Verbeeck, A.E., and Chambaere, D.G. (1985) Influence of small aluminum substitutions on the hematite lattice. Physics Letters A, 107, 181-184.

Dyar, M.D., Agresti, D.G., Schaefer, M.W., Grant, C.A., and Sklute, E.C. (2006) Mössbauer spectroscopy of earth and planetary materials. Annual Review of Earth and Planetary Sciences, 34, 83-125.

Fei, Y., Virgo, D., Mysen, B.O., Wang, Y., and Mao, H.K. (1994) Temperature-dependent electron delocalization in $(Mg,Fe)SiO_3$ perovskite. American Mineralogist, 79, 826-837.

Frauenfelder H. 1962. The Mössbauer effect. New York: WA Benjamin, p. 333.

Frost, D.J., and Langenhorst, F. (2002) The effect of Al_2O_3 on Fe-Mg partitioning between magnesiowustite and magnesium silicate perovskite. Earth and Planetary Science Letters, 199, 227-241.

Frost, D.J., Liebske, C., Langenhorst, F., McCammon, C.A., Tronnes, R.G., and Rubie, D.C. (2004) Experimental evidence for the existence of iron-rich metal in the Earth's lower mantle. Nature, 428, 409-412.

Fujino, K., Nishio-Hamane, D., Seto, Y., Sata, N., Nagai, T., Shinmei, T., Irifune, T., Ishii, H., Hiraoka, N., Cai, Y.Q., and Tsuei, K.D. (2012) Spin transition of ferric

Always consult and cite the final, published document. See http://www.minsocam.org or GeoscienceWorld

iron in Al-bearing Mg-perovskite up to 200 GPa and its implication for the lower mantle. Earth and Planetary Science Letters, 317, 407-412.

Grocholski, B., Shim, S.H., Sturhahn, W., Zhao, J., Xiao, Y., and Chow, P.C. (2009) Spin and valence states of iron in $(Mg_{0.8}Fe_{0.2})SiO_3$ perovskite. Geophysical Research Letters, 36, L24303.

Hsu, H., Umemoto, K., Blaha, P., and Wentzcovitch, R.M. (2010) Spin states and hyperfine interactions of iron in $(Mg,Fe)SiO_3$ perovskite under pressure. Earth and Planetary Science Letters, 294, 19-26.

Hummer, D.R., and Fei, Y.W. (2012) Synthesis and crystal chemistry of Fe^{3+}-bearing $(Mg,Fe^{3+})(Si,Fe^{3+})O_3$ perovskite. American Mineralogist, 97, 1915-1921.

Jackson, J.M., Sturhahn, W., Shen, G.Y., Zhao, J.Y., Hu, M.Y., Errandonea, D., Bass, J.D., and Fei, Y.W. (2005) A synchrotron Mössbauer spectroscopy study of $(Mg,Fe)SiO_3$ perovskite up to 120 GPa. American Mineralogist, 90, 199-205.

Katsura, T., Sato, K., Ito, E., 1998. Electrical conductivity of silicate perovskite at lower-mantle conditions. Nature 395, 493-495.

Kupenko, I., McCammon, C., Sinmyo, R., Prescher, C., Chumakov, A.I., Kantor, A., Ruffer, R., and Dubrovinsky, L. (2014) Electronic spin state of Fe,Al-containing $MgSiO_3$ perovskite at lower mantle conditions. Lithos, 189, 167-172.

Lagarec, K., and Rancourt, D.G. (1997) Extended Voigt-based analytic lineshape method for determining N-dimensional correlated hyperfine parameter distributions in Mössbauer spectroscopy. Nuclear Instruments & Methods in Physics Research Section B-Beam Interactions with Materials and Atoms, 129, 266-280.

Always consult and cite the final, published document. See http://www.minsocam.org or GeoscienceWorld

Lauterbach, S., McCammon, C.A., van Aken, P., Langenhorst, F., and Seifert, F. (2000) Mössbauer and ELNES spectroscopy of (Mg,Fe)(Si,Al)O_3 perovskite: a highly oxidised component of the lower mantle. Contributions to Mineralogy and Petrology, 138, 17-26.

Li, J., Struzhkin, V.V., Mao, H.K., Shu, J.F., Hemley, R.J., Fei, Y.W., Mysen, B., Dera, P., Prakapenka, V., and Shen, G.Y. (2004) Electronic spin state of iron in lower mantle perovskite. Proceedings of the National Academy of Sciences of the United States of America, 101, 14027-14030.

Li, J., Sturhahn, W., Jackson, J.M., Struzhkin, V.V., Lin, J.F., Zhao, J., Mao, H.K., and Shen, G. (2006) Pressure effect on the electronic structure of iron in (Mg,Fe)(Si,Al)O_3 perovskite: a combined synchrotron Mössbauer and X-ray emission spectroscopy study up to 100 GPa. Physics and Chemistry of Minerals, 33, 575-585.

Li, J. (2007) Electronic transitions and spin states in the lower mantle. Post-perovskite: the last mantle phase transition, 174, 47-68.

Lin, J.F., Alp, E.E., Mao, Z., Inoue, T., McCammon, C., Xia, Y.M., Chow, P., and Zhao, J.Y. (2012) Electronic spin states of ferric and ferrous iron in the lower-mantle silicate perovskite. American Mineralogist, 97, 592-597.

Lin, J.F., Watson, H., Vanko, G., Alp, E.E., Prakapenka, V.B., Dera, P., Struzhkin, V.V., Kubo, A., Zhao, J.Y., McCammon, C., and Evans, W.J. (2008) Intermediate-spin ferrous iron in lowermost mantle post-perovskite and perovskite. Nature Geoscience, 1, 688-691.

Always consult and cite the final, published document. See http://www.minsocam.org or GeoscienceWorld

Lin, J.F., Speziale, S., Mao, Z., and Marquardt, H. (2013) Effects of the electronic spin transitions of iron in lower mantle minerals: implications for deep mantle geophysics and geochemistry. Reviews of Geophysics, 51, 244-275.

Lundin, S., Catalli, K., Santillan, J., Shim, S.H., Prakapenka, V.B., Kunz, M., and Meng, Y. (2008) Effect of Fe on the equation of state of mantle silicate perovskite over 1 Mbar. Physics of the Earth and Planetary Interiors, 168, 97-102.

McCammon, C. (1997) Perovskite as a possible sink for ferric iron in the lower mantle. Nature, 387, 694-696.

McCammon, C. (1998) The crystal chemistry of ferric iron in $Fe_{0.05}Mg_{0.95}SiO_3$ perovskite as determined by Mössbauer spectroscopy in the temperature range 80-293 K. Physics and Chemistry of Minerals, 25, 292-300.

McCammon, C., Kantor, I., Narygina, O., Rouquette, J., Ponkratz, U., Sergueev, I., Mezouar, M., Prakapenka, V., and Dubrovinsky, L. (2008) Stable intermediate-spin ferrous iron in lower-mantle perovskite. Nature Geoscience, 1, 684-687.

McCammon, C., Dubrovinsky, L., Narygina, O., Kantor, I., Wu, X., Glazyrin, K., Sergueev, I., and Chumakov, A.I. (2010) Low-spin Fe^{2+} in silicate perovskite and a possible layer at the base of the lower mantle. Physics of the Earth and Planetary Interiors, 180, 215-221.

Narygina, O.V., Kantor, I.Y., McCammon, C.A., and Dubrovinsky, L.S. (2010) Electronic state of Fe^{2+} in $(Mg,Fe)(Si,Al)O_3$ perovskite and $(Mg,Fe)SiO_3$ majorite at pressures up to 81 GPa and temperatures up to 800 K. Physics and Chemistry of Minerals, 37, 407-415.

Always consult and cite the final, published document. See http://www.minsocam.org or GeoscienceWorld

Narygina, O.V., Mattesini, M., Kantor, I., Pascarelli, S., Wu, X., Aquilanti, G., McCammon, C., and Dubrovinsky, L. (2009) High-pressure experimental and computational XANES studies of $(Mg,Fe)(Si,Al)O_3$ perovskite and (Mg,Fe)O ferropericlase as in the Earth's lower mantle. Physical Review B, 79, 174115.

Potapkin, V., McCammon, C., Glazyrin, K., Kantor, A., Kupenko, I., Prescher, C., Sinmyo, R., Smirnov, G.V., Chumakov, A.I., Ruffer, R., and Dubrovinsky, L. (2013) Effect of iron oxidation state on the electrical conductivity of the Earth's lower mantle. Nature Communications, 4, 1427.

Pound, R.V., and Rebka, G.A. (1960) Variation with temperature of the energy of recoil-free gamma-rays from solids. Physical Review Letters, 4, 274-275.

Prescher, C., McCammon, C., and Dubrovinsky, L. (2012) MossA: a program for analyzing energy-domain Mössbauer spectra from conventional and synchrotron sources. Journal of Applied Crystallography, 45, 329-331.

Richmond, N.C., and Brodholt, J.P. (1998) Calculated role of aluminum in the incorporation of ferric iron into magnesium silicate perovskite. American Mineralogist, 83, 947-951.

Smyth, D.M. (1993) Oxidative nonstoichiometry in Perovskite oxides. In: Tejuco, L.G., Fierro, J.L.G., Eds., Properties and Applications of Perovskite-Type Oxides, p. 47-72. Marcel Dekker, New York.

Vanpeteghem, C.B., Angel, R.J., Ross, N.L., Jacobsen, S.D., Dobson, D.P., Litasov, K.D., and Ohtani, E. (2006) Al, Fe substitution in the $MgSiO_3$ perovskite structure: a single-crystal X-ray diffraction study. Physics of the Earth and Planetary Interiors, 155, 96-103.

Always consult and cite the final, published document. See http://www.minsocam.org or GeoscienceWorld

Wood, B.J., and Rubie, D.C. (1996) The effect of alumina on phase transformations at the 660-kilometer discontinuity from Fe-Mg partitioning experiments. Science, 273, 1522-1524.

Wright, K., and Price, G.D. (1989) Computer-Simulations of Iron in Magnesium-Silicate Perovskite. Geophysical Research Letters, 16, 1399-1402.

Xu, Y.S., McCammon, C., and Poe, B.T. (1998) The effect of alumina on the electrical conductivity of silicate perovskite. Science, 282, 922-924.

Xu, Y.S., McCammon, C., 2002. Evidence for ionic conductivity in lower mantle $(Mg,Fe)(Si,Al)O_3$ perovskite. Journal of Geophysical Research, 107, 2251.

Always consult and cite the final, published document. See http://www.minsocam.org or GeoscienceWorld

462 **Figure Captions**

463 **Figure 1.** Mössbauer spectra of $Mg_{0.868}Fe_{0.087}Si_{0.944}Al_{0.101}O_{2.994}$ bridgmanite between 65
464 K and 300 K at 1 bar. Each spectrum (black dots) was fitted by four doublets (black
465 envelop): Fe^{3+} (green solid), Fe^{2+}I (blue dotted), Fe^{2+}II (red dashed) and Fe^{2+}III (gray
466 filled). Red dots represent the fitting residual. Within the velocity range of our
467 measurements, a sextet from metallic Fe would consist of peaks near -3.0, -1.0, 1.0, and
468 3.0 mm/s.

469 **Figure 2.** Area fractions (a, b) and hyperfine parameters (c, d) of iron sites in
470 $Mg_{0.868}Fe_{0.087}Si_{0.944}Al_{0.101}O_{2.994}$ bridgmanite as a function of temperature at 1 bar. The
471 iron sites include Fe^{2+}I (open squares), Fe^{2+}II (open circles), Fe^{2+}III (gray triangles), and
472 Fe^{3+}(solid diamonds). In (d), the curves represent the Debye model fittings for the
473 weighted average of Fe^{2+}I and Fe^{2+}II (solid), Fe^{2+}III (dashed), and Fe^{3+}(gray dotted).

474 **Figure 3.** Calculated recoil-free fractions as a function of temperature, according to the
475 Debye model. Red solid and dashed curves represent Fe^{2+} and Fe^{3+}, respectively, in Al-
476 Bm from this study; Gray solid and dashed curves represent Fe^{2+} and Fe^{3+}, respectively,
477 in Al-free Bm from McCammon (1998).

478 **Figure 4.** Ternary diagram illustrating the cation substitution mechanisms in bridgmanite
479 in full compositional range (a) and a close-up (b). The end-member compositions Si_2O_4,
480 $(Mg,Fe^{2+})_2O_2$, and $(Fe^{3+},Al)_2O_3$ are written on the two-cation basis. Lines connecting the
481 trivalent-cation-free composition $(Mg, Fe^{2+})SiO_3$ to each of the three trivalent-bearing
482 compositions represent (1) $(Mg,Fe^{2+})(Fe^{3+},Al)O_{2.5}$, oxygen vacancy substitution
483 mechanism, (2) $(Fe^{3+},Al)_2O_3$, coupled substitution mechanism, and (3) $(Fe^{3+},Al)SiO_{3.5}$,
484 cation vacancy substitution mechanism. Open and closed symbols represent Al-free and

Always consult and cite the final, published document. See http://www.minsocam.org or GeoscienceWorld

485 Al-bearing compositions, respectively. Error bars in this study are smaller than the
486 symbol size. More complex compositions including cations other than Mg, Si, Al, and Fe
487 are not included.

Always consult and cite the final, published document. See http://www.minsocam.org or GeoscienceWorld

Table 1. Hyperfine parameters of $Mg_{0.868}Fe_{0.087}Si_{0.944}Al_{0.101}O_{2.994}$ bridgmanite at 1 bar.

	Fe^{2+}I				Fe^{2+}II				
T (K)	QS (mm/s)	CS (mm/s)	FWHM (mm/s)	A[a] (%)	QS (mm/s)	CS (mm/s)	FWHM (mm/s)	A[a] (%)	
65	2.80(2)	1.051(6)	0.44(4)	31(4)	1.8(5)	1.17(5)	1.2(3)	14(7)	
100	2.76(1)	1.039(4)	0.37(3)	27(2)	1.8(1)	1.13(2)	0.9(1)	20(3)	
150	2.72(2)	1.004(4)	0.38(3)	23(3)	1.80(8)	1.09(1)	0.76(6)	25(3)	
200	2.67(2)	0.962(5)	0.36(4)	17(3)	1.78(6)	1.048(8)	0.73(4)	33(3)	
250	2.61(3)	0.924(9)	0.36(6)	11(3)	1.78(6)	1.000(8)	0.75(4)	39(3)	
300	2.55(4)	0.89(1)	0.32(9)	5(3)	1.72(4)	0.956(7)	0.75(3)	44(2)	
	Fe^{2+}III				Fe^{3+}				
T (K)	QS (mm/s)	CS (mm/s)	FWHM (mm/s)	A[a] (%)	QS (mm/s)	CS (mm/s)	FWHM (mm/s)	A[a] (%)	Fraction[b] (%)
65	4.03(3)	1.11(2)	0.34(7)	6(1)	0.89(1)	0.407(7)	0.52(1)	49(5)	46(5)
100	3.97(3)	1.12(1)	0.32(5)	6(1)	0.897(8)	0.397(5)	0.449(9)	48(3)	45(3)
150	3.86(4)	1.11(2)	0.30(6)	4(1)	0.898(9)	0.372(5)	0.439(9)	48(2)	48(2)
200	3.74(5)	1.11(2)	0.28(8)	3(1)	0.902(9)	0.339(5)	0.437(9)	47(2)	44(2)
250	3.55(5)	1.09(2)	0.20(8)	1(1)	0.91(1)	0.306(6)	0.47 (1)	48(3)	45(3)
300	3.47(9)	1.06(4)	0.2(1)	1(1)	0.91(1)	0.306(6)	0.47 (1)	48(3)	46(2)

CS: Center shift. QS: Quadruple splitting. FWHM: Full width at half maximum.
[a]Area Fractions. [b]Molar fractions. Numbers in parentheses represent fitting errors.

Table 2. Debye parameters and recoil-free fractions of bridgmanites at 1 bar.

Site	Composition	Θ_D (K)	δ_I (mm/s)	$f_{300\,K}$
Fe^{2+}	**Fe_9Al_{10} (this study)**	**305(3)**	**1.096(5)**	**0.637(6)**
	Fe_{10} (Fei)	233	1.304	0.47
	Fe_5 (Fei)	405	1.264	0.77
	Fe_5 (McC)	366	1.259	0.73
Fe^{2+} large QS	**Fe_9Al_{10} (Liu)**	**1102(114)**	**1.115(4)**	**0.956(4)**
Fe^{3+}	**Fe_9Al_{10} (this study)**	**361(22)**	**0.412(4)**	**0.72(2)**
	Fe_{10} (Fei)	1553	0.426	0.97
	Fe_5 (Fei)	1366	0.430	0.97
	Fe_5 (McC)	476	0.426	0.82

Θ_D: Debye temperature. δ_I: Intrinsic isomer shift. $f_{300\,K}$: recoil-free fraction at 300 K.
Numbers in parentheses represent fitting errors.
Data sources: Fe_9Al_{10}(this study): $Mg_{0.868}Fe_{0.087}Si_{0.944}Al_{0.101}O_{2.994}$ from this study;
Fe_5 (Fei) and Fe_{10} (Fei): $Mg_{0.95}Fe_{0.05}SiO_3$ and $Mg_{0.90}Fe_{0.10}SiO_3$, respectively (Fei et al. 1994);
Fe_5 (McC): $Mg_{0.95}Fe_{0.05}SiO_3$ (McCammon 1998).

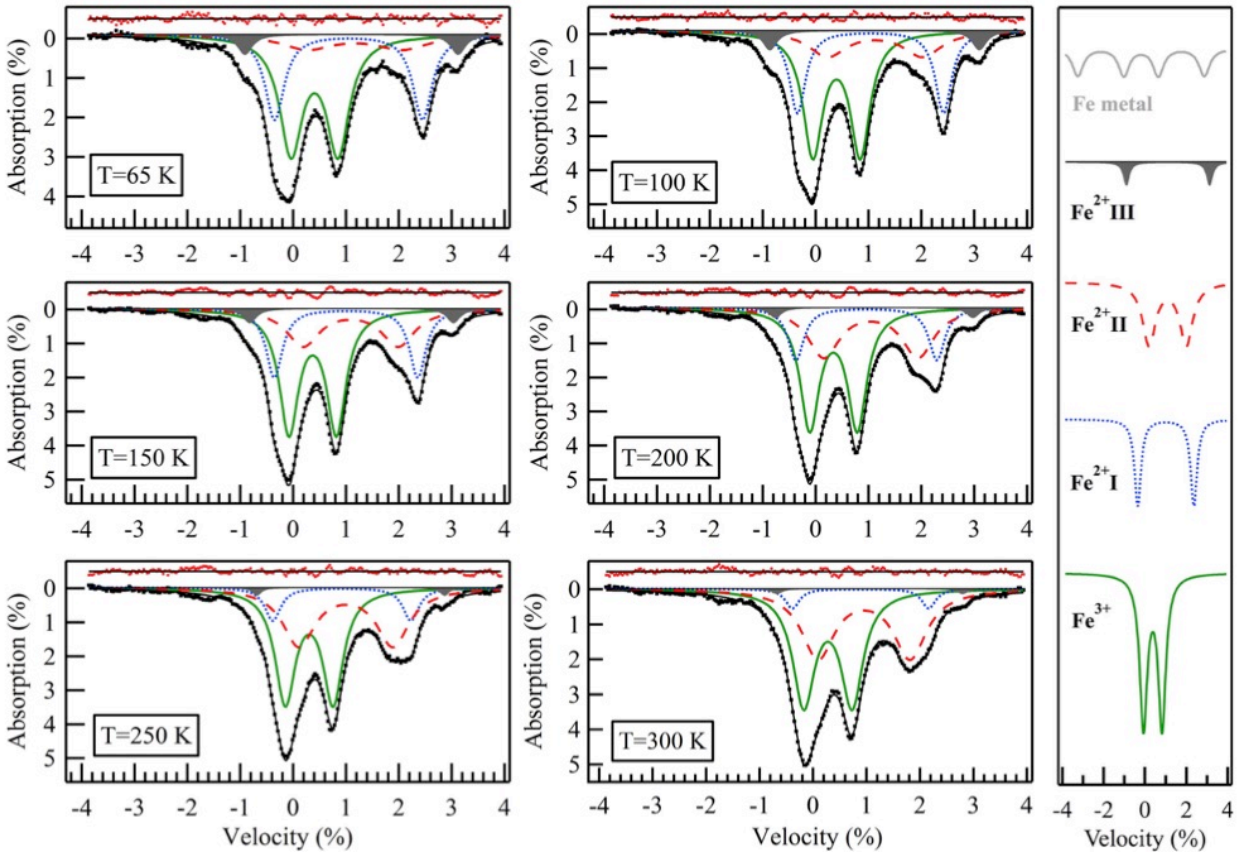

Figure 1. Mössbauer spectra of $Mg_{0.868}Fe_{0.087}Si_{0.944}Al_{0.101}O_{2.994}$ bridgmanite between 65 K and 300 K at 1 bar. Each spectrum (black dots) was fitted by four doublets (black envelop): Fe^{3+} (green solid), Fe^{2+}I (blue dotted), Fe^{2+}II (red dashed) and Fe^{2+}III (gray filled). Red dots represent the fitting residual. Within the velocity range of our measurements, a sextet from metallic Fe would consist of peaks near -3.0, -1.0, 1.0, and 3.0 mm/s.

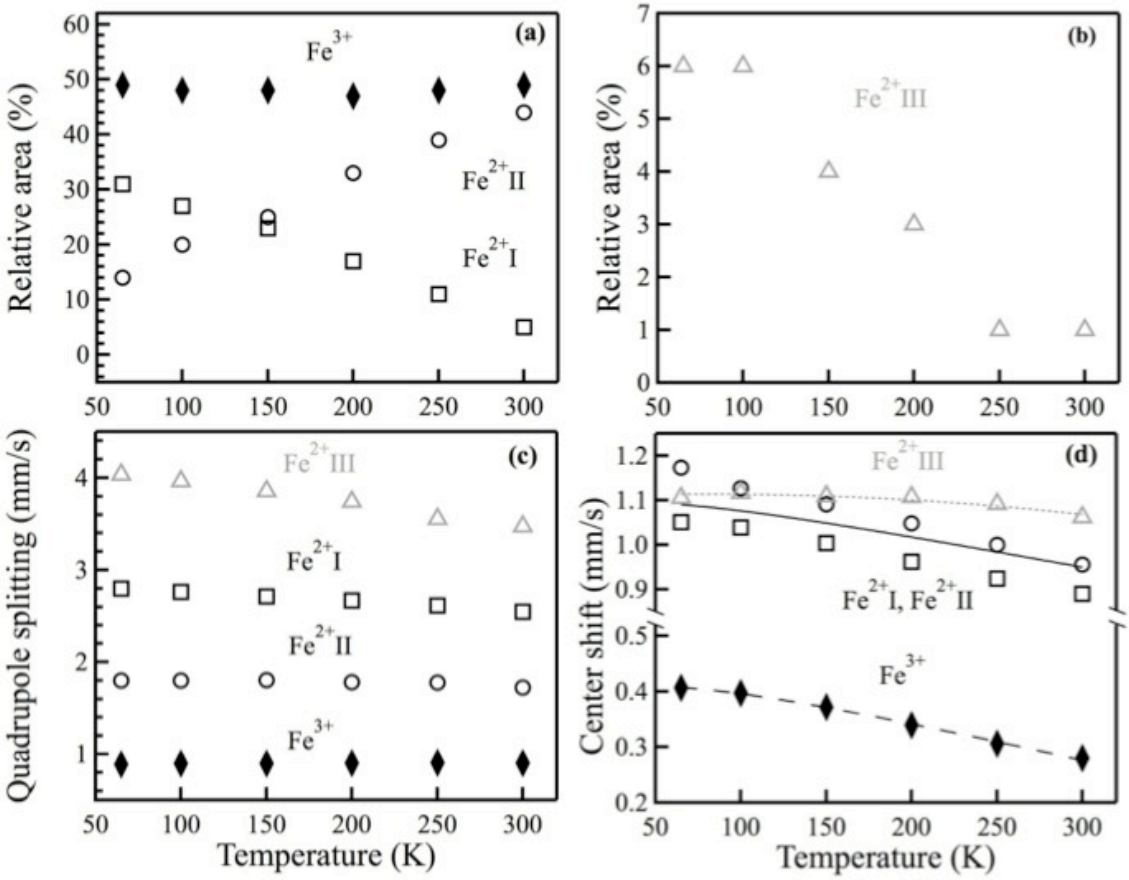

Figure 2. Area fractions (a, b) and hyperfine parameters (c, d) of iron sites in bridgmanite $Mg_{0.868}Fe_{0.087}Si_{0.944}Al_{0.101}O_{2.994}$ as a function of temperature at 1 bar. The iron sites include Fe^{2+}I (open squares), Fe^{2+}II (open circles), Fe^{2+}III (gray triangles), and Fe^{3+}(solid diamonds). In (d), the curves represent the Debye model fittings for the weighted average of Fe^{2+}I and Fe^{2+}II (solid), Fe^{2+}III (dashed), and Fe^{3+}(gray dotted).

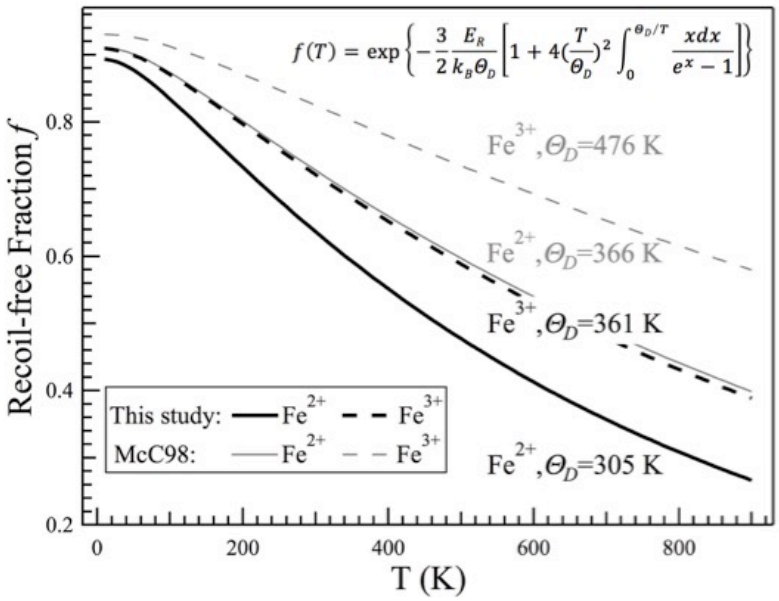

Figure 3. Calculated recoil-free fractions as a function of temperature, according to the Debye model. Black solid and dashed curves represent Fe^{2+} and Fe^{3+}, respectively, in Al-Bm from this study; Gray solid and dashed curves represent Fe^{2+} and Fe^{3+}, respectively, in Al-free Bm from McCammon (1998).

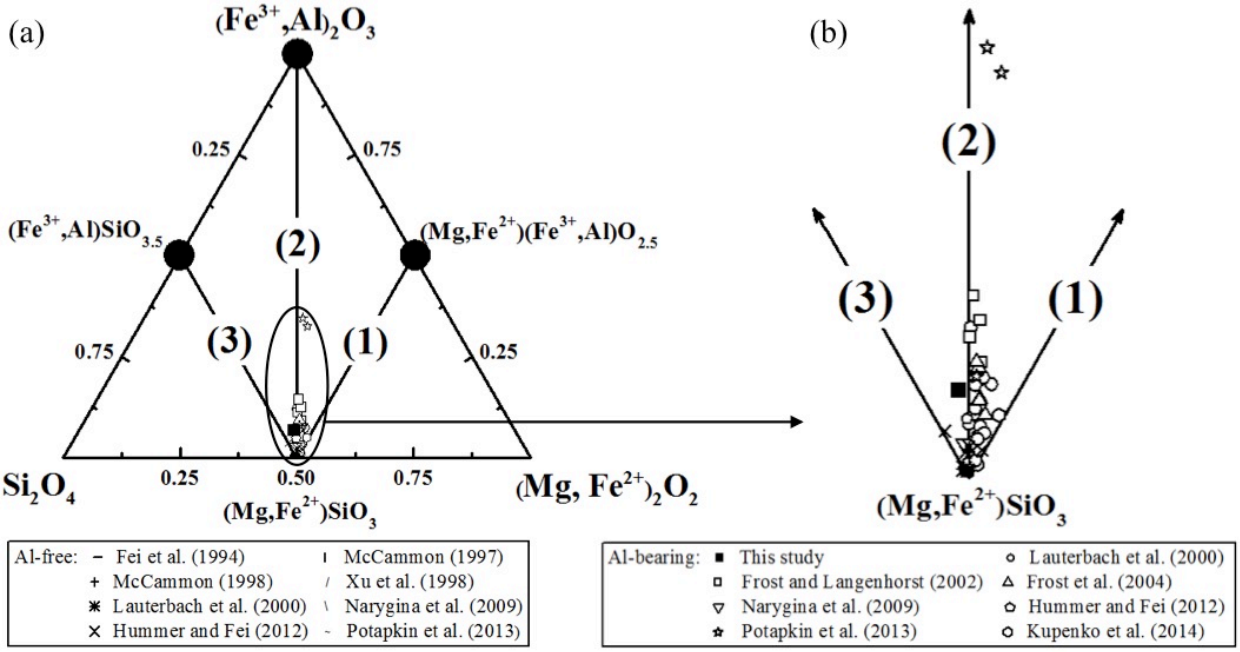

Figure 4. Ternary diagram illustrating the cation substitution mechanisms in bridgmanite in full compositional range (a) and a close-up (b). The end-member compositions Si_2O_4, $(Mg,Fe^{2+})_2O_2$, and $(Fe^{3+},Al)_2O_3$ are written on the two-cation basis. Lines connecting the trivalent-cation-free composition $(Mg, Fe^{2+})SiO_3$ to each of the three trivalent-bearing compositions represent (1) $(Mg,Fe^{2+})(Fe^{3+},Al)O_{2.5}$, oxygen vacancy substitution mechanism, (2) $(Fe^{3+},Al)_2O_3$, coupled substitution mechanism, and (3) $(Fe^{3+},Al)SiO_{3.5}$, cation vacancy substitution mechanism. Open and closed symbols represent Al-free and Al-bearing compositions, respectively. Error bars in this study are smaller than the symbol size. More complex compositions including cations other than Mg, Si, Al, and Fe are not included.